Stress-modulated composition in the vicinity of dislocations in nearly lattice matched $Al_xIn_{1-x}N$/GaN heterostructures: A possible explanation of defect insensitivity

Anas Mouti,[1,*] Jean-Luc Rouvière,[2] Marco Cantoni,[1] Jean-Francois Carlin,[3] Eric Feltin,[3] Nicolas Grandjean,[3] and Pierre Stadelmann[1]

[1]*Interdisciplinary Center of Electron Microscopy (CIME), EPFL, Lausanne, Switzerland*

[2]*CEA-INAC/UJF-Grenoble1 UMR-E, SP2M, LEMMA, Minatec Grenoble, France*

[3]*Institute of Condensed Matter Physics (ICMP), EPFL, Lausanne, Switzerland*

(Received 24 November 2010; revised manuscript received 2 February 2011; published 9 May 2011)

Evidence of composition fluctuations around threading dislocations at scales ranging from atomic distances to tens of nanometers is provided by *z*-contrast imaging, strain measurement, and energy dispersive x-ray spectroscopy in $Al_xIn_{1-x}N$/GaN heterostructures. The atomic core rings of edge-type dislocations are shown to lie across highly antisymmetric elemental environments, and the indium-rich pit centers of mixed dislocation are found to lie on the tensile side of their atomic core ring. The observed composition fluctuations around pure-edge dislocations are compared with an elastostatic free energy model calculation and a good qualitative and quantitative agreement is obtained. Hydrostatic stress is shown to be their principal cause: Tensile stress regions are indium rich and compressive stress regions are aluminum rich. We show that the stress field of a mixed dislocation can impact the composition of the alloy more than a hundred nanometers away from its core. Indium core segregation on pure-screw threading dislocation is also evidenced and explained by the model, as shear stress is also expected to affect composition. Furthermore, threading dislocations are shown to bend less in the $Al_xIn_{1-x}N$ alloy than in GaN, suggesting that they are "pinned" by stress-induced fluctuations. Such concentration modulations can have an important impact on optical and electrical properties of Group-III nitride devices that generally contain a high dislocation density (in the 10^8 to 10^{10} cm^{-2} range). We propose that stress-induced composition modulation could be the origin of defect insensitivity in indium-containing nitride ternary alloys.

DOI: 10.1103/PhysRevB.83.195309 PACS number(s): 61.72.uj, 61.43.−j, 61.72.Lk, 68.37.Ma

I. INTRODUCTION

Group-III nitrides, which have tunable band gaps spanning the entire visible spectrum, are very interesting semiconductors for their numerous potential applications in electronics and optoelectronics,[1–3] and also for more fundamental applications such as polariton lasing.[4] More recently, $Al_xIn_{1-x}N$ attracted some special attention due to the possibility of growing nearly lattice matched $Al_xIn_{1-x}N$/GaN heterostructures allowing the fabrication of crack-free and low threading dislocation (TD) density Bragg mirrors,[5,6] tunable interface strain high electron mobility transistors (HEMTs),[7] and infrared emitters based on intersubband transitions.[8] From a fundamental point of view, the most important characteristic of $Al_xIn_{1-x}N$ and $In_xGa_{1-x}N$ grown by metalorganic vapor phase epitaxy (MOVPE) is their dislocation-insensitive optical emission, which sparked a scientific debate with regard to its origin. Chichibu *et al.*[9] measured extremely short positron annihilation diffusion lengths as well as short radiative lifetimes in indium-containing Group-III nitrides, and explained their results by a possible localization of excitons around indium-rich atomic aggregates. In the case of $In_xGa_{1-x}N$, indium-rich clusters were observed[10–13] but a strong debate is still ongoing on whether they are real or electron-beam-generated artifacts.[13]

The best-known stress-related disorder in Group-III nitrides is V-shaped pit formation at layer surfaces and will be briefly described in this report. It was generally predicted at the intersection of dislocations with free surfaces by Frank in 1951,[14] as a consequence of elastic energy minimization by the introduction of extra surface facets to relax stress. Therefore pit formation at dislocation tips is expected whenever the energy balance favors extra surface creation during crystal growth (i.e., whenever the surface energy of the pit facets is inferior to the elastic energy lost by relaxing stress). Some threading dislocations are known to form pits in indium-containing Group-III nitride alloys and heterostructures.[15–17] However, some debate is going on about their origin. In $In_xGa_{1-x}N$ quantum well structures, Bright *et al.*[18] reported that they are formed by edge-component dislocations, while Kim *et al.*[15] reported screw-component dislocations as their source. Cho *et al.*[19] found pits generated by stacking mismatch boundaries (SMB) in low dislocation density $In_xGa_{1-x}N$ quantum well structures. In $Al_xIn_{1-x}N$, Miao *et al.*[16] reported pits with no dislocation at their origin in high indium content $Al_xIn_{1-x}N$ layers (23% In) by transmission electron microscope (TEM) imaging of cross-section images and attributed their origin to probable SMBs. However, this latter report is to be verified by further analysis as no experimental evidence of SMB presence underneath the TD-free pits was provided, and dislocations at the origin of pits might have been polished away in thin areas of the prepared cross-sectional TEM lamella. The latter possibility can also explain the fact that the reported dislocation-free pits were small and random in size.

Concerning compositional fluctuations in $Al_xIn_{1-x}N$, previous publications reported optical and low-range structural disorder in MOVPE-grown $Al_xIn_{1-x}N$/GaN heterostructures,[20,21] as well as long-range structural disorder in molecular beam epitaxy (MBE) grown $Al_xIn_{1-x}N$.[22] Kehagias *et al.*[21] reported indium segregation on pit dihedral angles (also shown in this paper) forming sixfold indium-rich "stars" in MOVPE-grown $Al_xIn_{1-x}N$ and explained its origin by strain relaxation inducing a higher surface energy and

thus favoring indium, which has a lower growth temperature. Zhou *et al.*[22] reported honeycomb structures with indium-rich walls along the *c* axis in MBE-grown $Al_xIn_{1-x}N$ samples and explained them in terms of phase separation, while Sahonta *et al.*[23] explained the same phenomenon in terms of indium segregation alongside the borders of growth islands. This latter effect is an MBE-related disorder, which is very different from the one reported in this paper, and thus will not be discussed further.

The lattice matching of $Al_xIn_{1-x}N$ removes many fundamental and practical complications for the analysis of the physics of its alloying composition. The small amount of interfacial strain is the key factor: It allows the growth of relatively thick layers (100–150 nm) with no significant defect creation and does not significantly perturb the stress fields of TDs. The implications of the latter factors are multiple: the possibility of analyzing by TEM or scanning TEM (STEM) pure $Al_xIn_{1-x}N$ prepared samples that are sufficiently thick to yield a good signal, the stress fields around the TDs—as not perturbed by a strong interfacial strain—can be compared to calculations, and finally layer bending and relaxation after sample preparation are minimized. $Al_xIn_{1-x}N$ can, for all of the enunciated reasons, be considered a school case for other Group-III nitride alloys. We report herein qualitative and quantitative characterization of composition around edge, screw, and mixed type TDs in lattice-matched $Al_xIn_{1-x}N$ and investigate the impact of stress on the alloy composition on scales ranging from atomic to tens of nanometers by comparing experimental results to an elastostatic model.

All of the studied dislocations in this paper are threading dislocations with a line along the *c* axis, and therefore we will indiscernibly use the terms dislocation (edge, mixed, screw) and TD to designate *c*-line threading dislocations. We also use the hexagonal lattice three-index notation for calculations and the four-index notation for generally treating crystallographic vectors, planes, and directions. We also define the "axis of maximum stress" (AMS) of an edge-type dislocation as the axis perpendicular to its line and to the edge component of its Burgers vector and passing through its core.

This paper starts by introducing the theory and the model used for calculations, presents the materials and techniques used for the study, and continues with experimental and calculation results followed by a discussion section and a conclusion.

II. THEORY AND MODELING

Although it is readily evident that indium (aluminum) should segregate where the lattice is under extension (compression), detailed calculations are necessary for a quantitative analysis of the observed contrast, strain, or elemental composition around dislocations. Such calculations were carried out using an elastostatic free energy model at thermodynamic equilibrium, considering AlN as a solvent and approximating InN unit cells by spherical elastic inhomogeneities (or inclusions). The total interaction energy (E_{tot}), to the second order, between a spherical inhomogeneity and a stress field can be expressed as[24]

$$E_{\text{tot}} = \frac{p^A \delta V}{3} + \frac{v'}{2}\left(\frac{B-B'}{9B^2}\frac{4\mu+3B}{4\mu+3B'}p^A p^A + \frac{15(\mu'-\mu)(1-\nu)}{2\mu[(\mu-\mu')(4-5\nu)-15\mu(1-\nu)]}{}^{\backprime}p^A_{ij}\,{}^{\backprime}p^A_{ij}\right), \quad (1)$$

where the summation convention is employed, p^A is the trace of the applied stress field tensor or hydrostatic stress (p^A_{mm}), ${}^{\backprime}p^A_{ij} = p^A_{ij} - \frac{1}{3}p^A\delta_{ij}$ is its deviatoric or shear part, and B, μ, and ν are the bulk modulus, shear modulus, and Poisson's ratio, respectively. The constants of the inhomogeneity are marked by an apostrophe, and δV, the confined volume of the inhomogeneity, is expressed as[25]

$$\delta V \cong (v'-v)\frac{1+(\frac{4\mu}{3B})}{1+(\frac{4\mu}{3B'})} = \alpha(v'-v), \quad (2)$$

where α is defined by the equation, and v and v' are the volumes of the AlN and InN unit cells, respectively, in our case. The inhomogeneity model is isotropic, which is sufficient in our case, since the studied directions in this paper are in plan view and therefore belong to the *c* plane, which is elastically isotropic in a wurtzite crystal.

Following Hirth and Lothe[25] we can calculate the expected InN atomic percentage concentration (**c**) around a dislocation using

$$\mathbf{c} = 100/\{1+\exp[-(E_{\text{tot}}+G_0)/(k_BT)]\}, \quad (3)$$

where $G_0 = k_BT\ln(\frac{\mathbf{c}_0}{100-\mathbf{c}_0})$ is an approximation of the chemical potential at null pressure, c_0 being the initial or rest concentration (20% atomic InN in our case), T the growth temperature in kelvins, and k_B Boltzmann's constant. Equation (3) is sometimes referred to as the Fermi-Dirac distribution for the obvious similarity with the fermion distribution equation.

The first term of the interaction energy [Eq. (1)] is the first-order factor, and therefore the main driving force of stress-induced composition. It is the classical thermodynamic $p\delta V$ term, and combination with Eq. (3) yields the intuitively expected result enunciated at the beginning of this section: The larger indium atoms will tend to occupy tensile stress regions, and vice versa for the smaller aluminum atoms. As an edge dislocation divides the space around it into a compressive half space and a tensile one, an elemental asymmetry is expected around it and will be treated and calculated further in the paper. However, Eq. (1) also contains second-order terms in which deviatoric terms (shear strain) play a role. Thus even pure-screw dislocations, which only produce shear strain, are expected to affect the elemental composition of their vicinity. In fact, as will be presented later, indium segregation is expected at their core. The inhomogeneity does not produce any shear stress, and the nonzero elements of its stress field in the absence of image forces (i.e., if the distance separating the inhomogeneity from a free surface is large compared with its dimensions), in spherical coordinates, are given by[25]

$$-p'_{rr} = \frac{\mu'\delta v}{\pi r^3} \quad \text{and} \quad p'_{\theta\theta} = p'_{\phi\phi} = \frac{\mu'\delta v}{2\pi r^3}, \quad (4)$$

where δv is the strength of the expansion (i.e., the volume change if the inhomogeneity were rigid) and r is the radial

distance from the inclusion. As the three components sum up to zero, the trace of the stress tensor induced by the inhomogeneity (i.e., its hydrostatic stress) is zero. As hydrostatic pressure (as a sum term) as well as shear stress are the driving factors of Eq. (3), and since neither of the two is perturbed by an inhomogeneity, there is no need to perform an iterative procedure for the validity of the model if image forces are ignored. Dislocation stress field was calculated using the Eshelby-Read-Shockley anisotropic elasticity model;[26] it is then inserted in Eq. (1), then Eq. (3), to calculate the elemental distribution around a dislocation. To generate the expected stress field taking into account stress composition modulation, $Al_xIn_{1-x}N$ cells can also be considered as elastic inclusions and their confined lattice parameters can be derived (see Appendix) from a combination of Eq. (2) with Vegard's law:

$$a_i^{\mathrm{inc}}(\mathbf{c}) \cong \sqrt[3]{\alpha\ a_i^3(\mathbf{c}) + a_i^3(\mathbf{c_0})(1-\alpha)}, \tag{5}$$

where $a_i^{\mathrm{inc}}(\mathbf{c})$ is the confined lattice parameter of an inclusion of a $\mathbf{c}$ indium content ($i = 1$, 2, or 3 using three index notation), $a_i'(\mathbf{c})$ is the lattice parameter of the same inclusion obtained by Vegard's law, and $a_i(\mathbf{c_0})$ is the nominal reference lattice parameter, taken to be that of the crystal at the rest concentration ($Al_{0.8}In_{0.2}N$ in our case), also obtained by Vegard's law. Hydrostatic strain field is then approximated by the sum of the strain field in the inclusion-free medium with that of the inhomogeneities.[26] It is, in our case,

$$\epsilon_{ii}(\mathbf{c}) = \epsilon_{ii}(\mathbf{c_0}) + \frac{a_i^{\mathrm{inc}}(\mathbf{c}) - a_i(\mathbf{c_0})}{a_i(\mathbf{c_0})}, \tag{6}$$

where $\epsilon_{ii}(\mathbf{c})$ is any hydrostatic strain field component ($i = 1$, 2, or 3) taking inhomogeneities into account (i.e., elemental variations), and $\epsilon_{ii}(\mathbf{c_0})$ is the corresponding strain field component in the homogeneous material at the rest concentration. Table I summarizes the fundamental constants of AlN and GaN from which all constants used in our calculations can be deduced. The Burgers vector edge value for $Al_xIn_{1-x}N$ in the calculation is taken as GaN's a_1 parameter for the edge component (3.189 Å),[27] to adopt the lattice match hypothesis. This value corresponds to an indium content of about 17%.[28]

III. MATERIALS AND METHODS

The analyzed sample is a 100 nm thick $Al_xIn_{1-x}N$ nearly lattice matched (18%–20% InN) to a 2 μm GaN buffer layer grown on a sapphire substrate. Layers were grown along the c axis, using the conditions reported by Carlin and Ilegems.[6] Experimental observations were carried out using a FEI Titan scanning transmission electron microscope (STEM) with a probe spherical aberration corrector for atomic-scale imaging equipped with a high angle annular dark field detector (HAADF), a CM300 (S)TEM with an Oxford Instruments energy dispersive x-ray spectroscopy detector (EDX), and a CM20 TEM for weak-beam imaging. Cross-sectional lamellas were prepared with tripod diamond film polishing followed by argon milling using a Gatan PIPS equipped with a low-energy ion gun. The plan-view lamella, however, was prepared using a Carl Zeiss NVision 40 CrossBeam focused ion beam (FIB) instrument for sample flatness for STEM-HAADF quality and to minimize x-ray absorption and fluorescence artifacts (Cliff-Lorimer corrections were used for quantification). The surface of the region of interest was first protected by an electron beam induced 2 μm thick carbon layer, then matter around and below it was removed by ion milling. It was then lifted out and first thinned from the substrate side then from the surface side with a razing incidence angle compensating for beam shape, and a gradually decreasing beam energy (30 kV to 5 kV) and current, until it reached a thickness of about 50 nm. The lamella was finally cleaned with a 2 kV and subsequently a 1 kV ion beam and decontaminated with an oxygen plasma. The lamella remained relatively flat, meaning that the layer suffered little stress relaxation. Further care was taken to avoid measurement artifacts, as for medium-resolution (i.e., not at atomic scale) HAADF and EDX maps, the sample was tilted by an angle of about 6°–7° degrees off zone axis to avoid channeling contrasts. HAADF atomic maps were taken at the [001] zone axis; their high resolution and contrast are proofs of the quality of the lamella preparation. Strain was measured from the atomic resolution maps by geometric phase analysis (GPA) [31] using Rouvière's software[32] with a reciprocal space window diameter of about 1.5 nm^{-1}.

TABLE I. Lattice constants (a_i) in Å, elastic constants (C_{ij}), and bulk moduli (B) in GPa used for the composition and strain calculations.

Material	a_1	a_3	C_{11}	C_{12}	C_{13}	C_{33}	C_{44}	B
AlN[27,29]	3.112	4.982	345	123	120	395	188	201
InN[27,30]	3.54	5.705	190	104	121	182	10	141

IV. EXPERIMENTAL RESULTS AND CALCULATIONS

A. Cross-sectional study of interfaces, threading dislocations, and pits

Prior to plan-view analysis, the $Al_xIn_{1-x}N$ layer and dislocations were examined in cross section to investigate interface roughness, dislocation bending, defect creation, and surface pits. $Al_xIn_{1-x}N$/GaN interfaces were found to be flat at the atomic scale as can be seen on the HRTEM image, Fig. 1(a).

To perform a statistical analysis of pit generation in $Al_xIn_{1-x}N$ layers, we chose to analyze thick parts of the TEM lamella (100–150 nm, determined by electron energy loss spectroscopy) to minimize the risk of a dislocation being cut off by sample preparation, which might give a false impression of a dislocation-free pit. The method of choice for carrying out such an experiment is weak-beam dark-field microscopy (WB), which has the double advantage of a good resolution and contrast at imaging dislocation cores (crucial for analyzing thick layers), and a much smaller thickness fringe spacing than conventional bright or dark field imaging, the bending of which highlights thickness variations engendered by pits.

Pits were found to be generated by screw-component TDs, as illustrated by Fig. 1(b), taken at $g = (0002)(4g)$ WB conditions, for which the invisibility criterion implies that only screw-component dislocations are visible, and where all

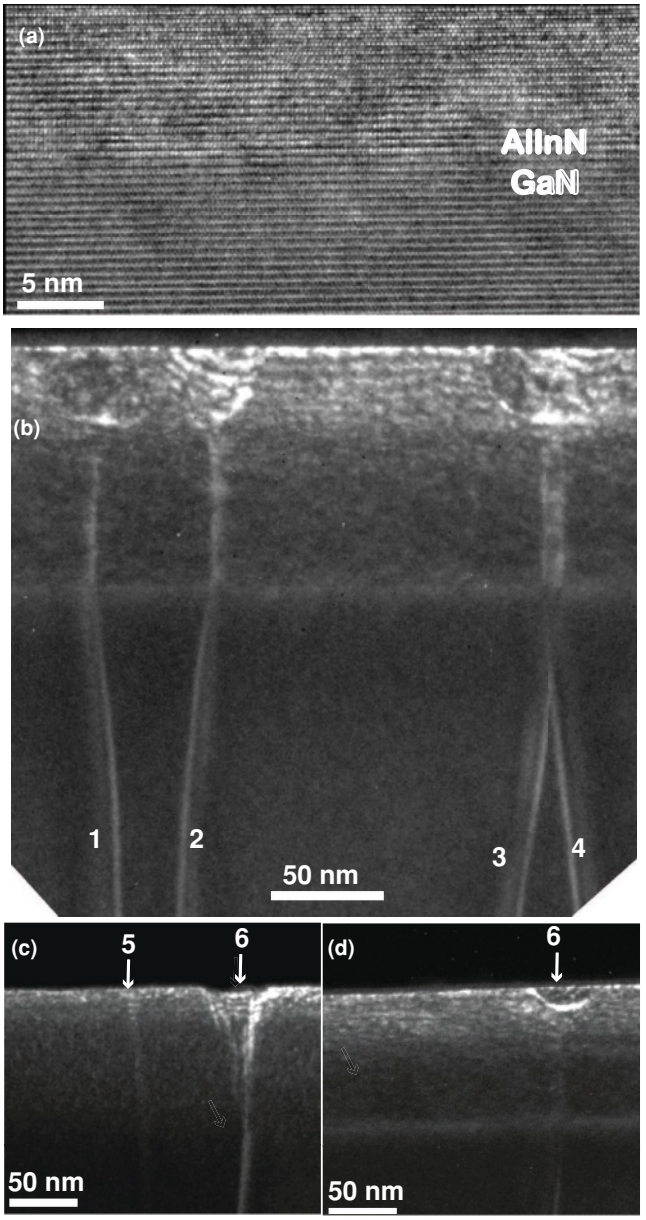

FIG. 1. (a) HRTEM image of the $Al_xIn_{1-x}N$/GaN interface along the $[1\bar{2}10]$ zone axis. (b) Cross-sectional weak-beam $g = (0002)(4g)$ micrograph of TDs in a 100 nm thick $Al_xIn_{1-x}N$ layer on a GaN buffer layer; only dislocations with Burgers vectors of the type $\langle 0001 \rangle$ are visible under these conditions, meaning visible TDs have a screw component. (c), (d) Weak-beam micrographs of the same region, in $g = (1\bar{1}00)(4g)$ condition (c), and $g = (0002)(4g)$ condition (d), in which TD edge and screw components are visible, respectively.

dislocations (numbers 1–4) generate surface pits. Figures 1(c) and 1(d) are $g = (\bar{1}100)(4g)$ and $g = (0002)(4g)$ images of the same area, highlighting respectively edge and screw components of the TDs. Dislocations 5 and 6 are visible in Fig. 1(c) so they both have an edge component, but only dislocation 6 is visible in Fig. 1(d), meaning that TD 5 is pure edge and TD 6 is mixed. Since only TD 6 generates a pit, this demonstrates that pit formation is due to the screw character.

One striking aspect of Fig. 1(b) is that dislocations bend in the GaN buffer layer but become straighter along the c axis once in the $Al_xIn_{1-x}N$ layer. This aspect was widely observed for TDs in our study and can also be seen for dislocation 6 in Figs. 1(c)–1(d). Dislocations in a majority of materials respond to stress by moving (gliding or climbing), but due to the absence of suitable gliding planes in Group-III nitrides, TD motion is energetically unfavorable and dislocations respond to stress by bending during growth to minimize their strain energy.[33,34] Thus, closely located dislocations respond to the influence of the stress field of each other by bending. This is the case of TDs 1 and 2 in the GaN buffer layer, which appear to repel each other, potentially meaning that their Burgers vectors are of a similar orientation, and TD 3 and 4, which appear to attract each other, suggesting their vectors are opposite in sign.[25] But why do all of them stop bending starting from the $Al_xIn_{1-x}N$ interface? One plausible reason is stress-induced composition modulation itself, as a ternary alloy such as $Al_xIn_{1-x}N$ offers the alternate possibility of minimizing strain energy by composition modulation. This effect is well known in metals and referred to as dislocation pinning, and widely used for increasing alloy hardness by introducing impurities to impede dislocation motion.[35] It was also studied theoretically and highlighted experimentally in semiconductors such as GaAs[36,37] and silicon.[38] Figures 1(b)–1(d) are thus in themselves pieces of evidence of stress-induced composition modulation in $Al_xIn_{1-x}N$.

We present in Secs. IV B, IV C, and IV D a plan-view study of strain and elemental composition in the vicinity of pure-edge, pure-screw, and mixed TDs, respectively. As pit sizes were found to vary in the plan-view observations (10–50 nm), we chose to study small pits for atomic resolution analysis and large pits for larger scales for clarity reasons.

B. Pure-edge threading dislocations

Figure 2(a) is a HAADF map at the center of which a pure-edge TD (Burgers vector $\mathbf{b} = 1/3\langle 11\bar{2}0 \rangle$) is located. A white arrow starting at the dislocation atomic core ring indicates the Burgers vector direction, and the axes directions taken for the analysis are drawn on the upper left side of the figure. The tensile (compressive) half space of the dislocation is located at the bottom (top) half of the figure. Contrast antisymmetry is readily noticeable: The tensile region of the TD appears brighter than the compressive one, and contrast is maximum near the atomic core ring and decreases continually with distance from it, suggesting the tensile side is richer in indium than the compressive one. The contrast is qualitatively in good agreement with the calculated elemental map of Fig. 2(b) as a strong antisymmetry occurs at the atomic core ring and decreases radially away from it. A diffraction contrast artifact can be ruled out since it would produce the inverse phenomenon (a crystal in compression diffracts at larger angles, and therefore would appear brighter in HAADF imaging). Channeling effects could also affect contrast around a dislocation, but Xin *et al.*[39] reported plan-view atomic-scale z-contrast imaging of edge dislocation cores in pure GaN, and no such contrast asymmetry between tensile and compressive regions is observable in their maps. However, to definitely rule

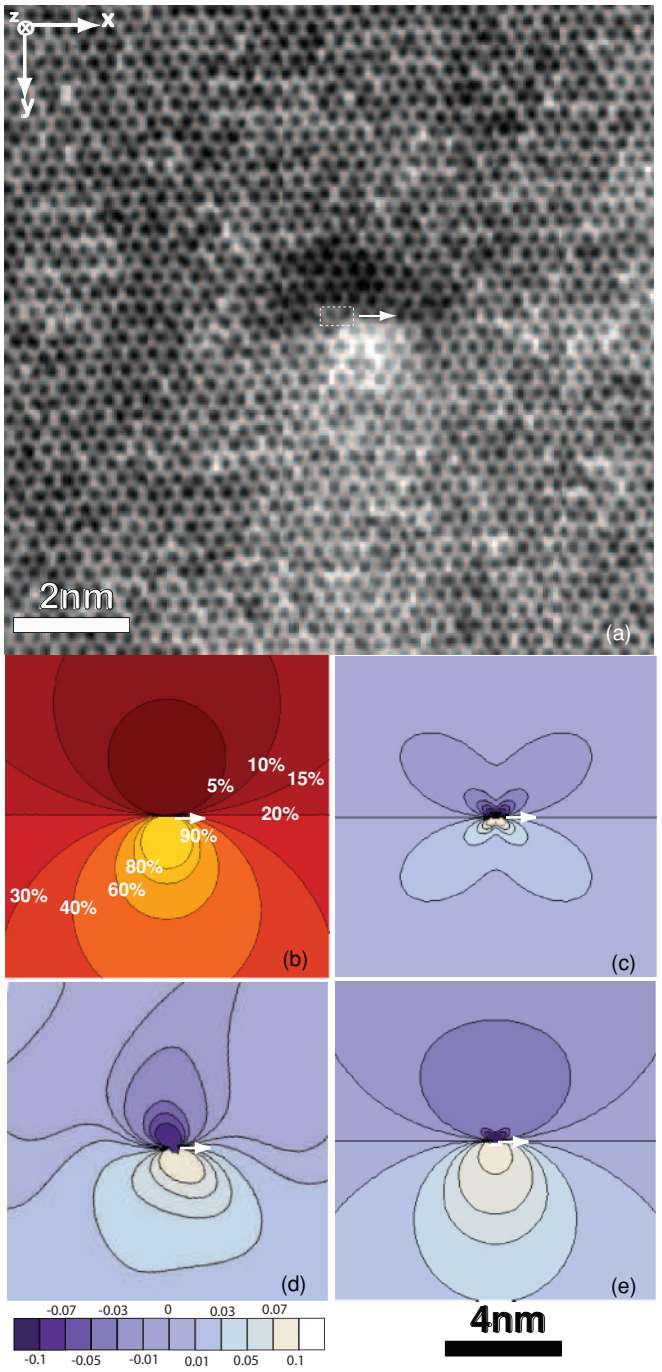

FIG. 2. (Color online) (a) Plan-view atomic-scale STEM-HAADF map of a pure-edge dislocation, showing contrast asymmetry around it. (b) Contour plot of simulated InN percentage around the dislocation. (c) Contour plot of simulated *x*-*x* strain around an edge dislocation in a homogeneous material using AlN elastic constants, showing the characteristic butterfly shape. (d) Contour plot of *x*-*x* strain of (a), obtained by GPA. (e) Simulated *x*-*x* strain taking into account indium segregation. The scale of the last four figures is indicated by the bottom scale bar, and the color coding of the strain maps by the bottom legend.

out the possibility of a contrast artifact, we use strain analysis as a second independent piece of evidence.

It is worth noting, for the rest of the analysis, that the bright contrast of the tensile half space (bottom half of the map) slightly bends toward the positive *x* direction (right).

Figure 2(c) is the calculated *x*-*x* strain map (ϵ_{xx}) of a pure-edge dislocation in a homogeneous AlN material, i.e., without any elemental fluctuation. Notice its characteristic perfectly antisymmetric butterfly shape (this butterfly shape is also visible experimentally in the strain maps of TDs in pure GaN, published by Kret *et al.*[40]). We used AlN elastic constants[29] for the calculation since AlN is the closest material to $Al_{0.8}In_{0.2}N$ with reported elastic constants; the amplitude of the strain field of a homogeneous $Al_{0.8}In_{0.2}N$ crystal should not be very different as even the use of the InN constants yields similar values and the exact same shape. The GPA measured strain in Fig. 2(d) is very different from that of Fig. 2(c), as it is much stronger and has a rounded aspect both at the tensile and compressive half spaces. Figure 2(d) is clearly more in agreement with the simulated strain field taking into account the indium segregation of Fig. 2(e), both qualitatively and quantitatively. Indeed, the strain field of Fig. 2(e) has a rounded shape like Fig. 2(d), especially on the tensile region, because of the lattice dilatation introduced by the indium inhomogeneities. The strain of Fig. 2(e) thus inherits the shape of the indium distribution of Fig. 2(b). Furthermore, the strength of the measured strain field [Fig. 2(d)], on the tensile side, and like the bright contrast of Fig. 2(a), slightly bends to the positive *x* direction (right), therefore definitely ruling out the possibility of contrast artifacts such as channeling or surface contamination. Quantitative agreement between Figs. 2(d) and 2(e), however, fails on the immediate atomic core ring vicinity of the compressive side of the dislocation. Indeed, since nominal indium concentration is about 20%, a high lattice deformation is expected on the tensile side, as InN can rise by a factor of 5 (20% to 100%). On the compressive side, however, InN content can fall by a maximum factor of 1 (20% to 0%); therefore indium depletion is expected to yield a smaller deformation on the compressive side, and the calculated stress field of Fig. 2(e) gradually takes the butterfly shape and amplitude of a dislocation in a homogeneous crystal [Fig. 2(c)] as the indium content falls to zero. The latter effect is not observed experimentally, as the compressive strain field is much stronger than the simulation at a distance of about 2 nm away from the atomic core ring and takes a rounded shape. This discrepancy is evidence of vacancy segregation on the compressive side of edge dislocation cores and will be treated in a future communication.

Since the simulated indium distribution shown in Fig. 2(b) predicts a full InN segregation on the tensile part of the dislocation core, and since its corresponding strain map [Fig. 2(e)] is consistent with the GPA measurements [Fig. 2(d)], we expect full InN segregation on edge dislocation cores. As GPA was found to be reliable for measuring subangtrom displacements from HRTEM images[41] and STEM-HAADF has also lately proved successful in accurately measuring subangstrom lattice distortions,[42] we consider the quantitative agreement between the strain measurement and the calculation as a solid validation of our model and of the occurrence of stress-induced compositional modulation in $Al_xIn_{1-x}N$.

It is very interesting to notice that the contrast maximum (thus potentially the In maximum) is not exactly at the

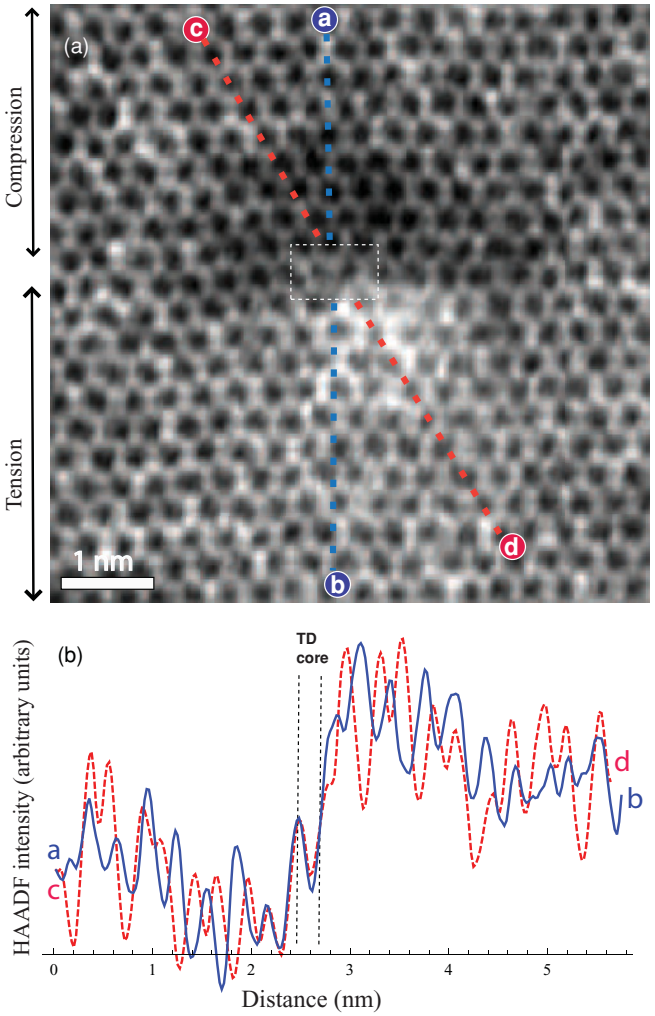

FIG. 3. (Color online) (a) Magnified z-contrast image of the dislocation core environment of Fig. 2(a); the core is indicated by a dotted white rectangle. (b) HAADF intensity profile between points a and b (blue) and points c and d (dotted and red) of (a).

dislocation atomic core ring, but shifted away from it by a few atomic distances. This is better shown by Fig. 3(a), which is a magnification of the core environment of the TD of Fig. 2 for improved clarity of the immediate elemental environment. The atomic core ring of an edge-component dislocation is expected to lie on a hydrostatic stress inflection point, since stress abruptly changes from compression to tension across it, especially on the AMS. Therefore, it should also lie on a composition inflection point, since composition was shown to be mainly hydrostatic stress driven in the pure-edge dislocation vicinity. This is verified by the two HAADF intensity profiles of Fig. 3(a) along two different directions: from point a to b and from point d to c. The TD atomic core ring lies indeed on a contrast inflection point and the contrast maximum and minimum are located at about 7 Å away from it. Finally, note in Fig. 3(a) that the atomic core ring of the dislocation has an eightfold ring structure as reported by Xin *et al.*[39]

C. Pure-screw threading dislocations

As was briefly mentioned in the theory section, shear stress plays a second-order role in the interaction energy of an inclusion with an applied stress field [Eq. (1)]; thus even pure-screw dislocations are expected by Eq. (3) to have an effect on their surrounding elemental composition. This is investigated in Fig. 4, which features in (a) a HAADF map of a pure-screw dislocation pit, showing a "star shape" similar to the one reported by Kehagias *et al.*,[21] a bright star shape along the pit angles, at crystallographic directions $\langle 11\bar{2}0\rangle$ between $(10\bar{1}1)$ sidewalls. Also, Fig. 4(b) is a larger field of view HAADF map of the same dislocation, in which some nanoscale disorder is present, but no contrast antisymmetry outside the pit is observable.

Figure 4(c) is a hydrostatic c-plane biaxial strain map ($\epsilon_{xx} + \epsilon_{yy}$) of Fig. 4(a); as the map is continuous everywhere, it can be concluded that the dislocation generating the pit is of a pure-screw character. The star shape of Fig. 4(a) is also visible in the strain map [Fig. 4(b)] with a higher lattice parameter (positive strain), thus confirming that the pit angles and core are indium rich. It is worth noting that the strain map suggests that the pit sidewalls in between the star-shape branches are poorer in indium that the outside environment of the pit, suggesting that the indium-rich branches (In-rich pit angles) "pump" indium out of their immediate surroundings.

The TD core seems, from the strain map, richest in indium, in agreement with the calculated map in Fig. 4(c) and the molecular dynamics simulation of Lei *et al.*[43] The calculation of Fig. 4(d) predicts a sharp radial indium increase at the pure-screw TD core. Indeed, the In equilibrium atomic concentration of $Al_xIn_{1-x}N$ is taken to be 20% in the model and indium is calculated to rise from 21% to 90% over just 5 nm. As the composition of the star-shape branches does not seem to follow (by z contrast and GPA) a sharp radial decrease away from the dislocation core, it is probably not stress related.

The fact that the star branches dilate the lattice (i.e., appear on the strain map) indicates that their extra indium content is not only located at the surface (pit angles) but is distributed two-dimensionally over the c axis: The star shapes are thus three-dimensional objects possibly similar to the drawing of Fig. 4(e), in which they are represented in purple, in top- and side-view perspectives.

Northrup *et al.*[44] found by *ab initio* calculation that indium core segregation is necessary to form pits on screw-type dislocations in $In_xGa_{1-x}N$. As the model presented herein does not use any specific aspect of $Al_xIn_{1-x}N$, it is plausibly applicable to MOVPE $In_xGa_{1-x}N$ and could be proposed as a source of In segregation that eventually leads to pit formation in In-containing ternary nitride alloys.

D. Mixed threading dislocations

Mixed dislocations ($\mathbf{b} = 1/3\langle 11\bar{2}3\rangle$) behave at the pit level in a very similar way to pure-screw dislocations: They generate indium-rich star shapes. Figure 5(a) and 5(b) are a HRSTEM HAADF map of a mixed TD pit and its GPA strain map, respectively. In Fig. 5(a) the star-shape branches are indicated with numbered arrows, the TD core highlighted by a dotted square, and the Burgers vector direction indicated by an arrow starting at the TD core. The star-shape branches are also

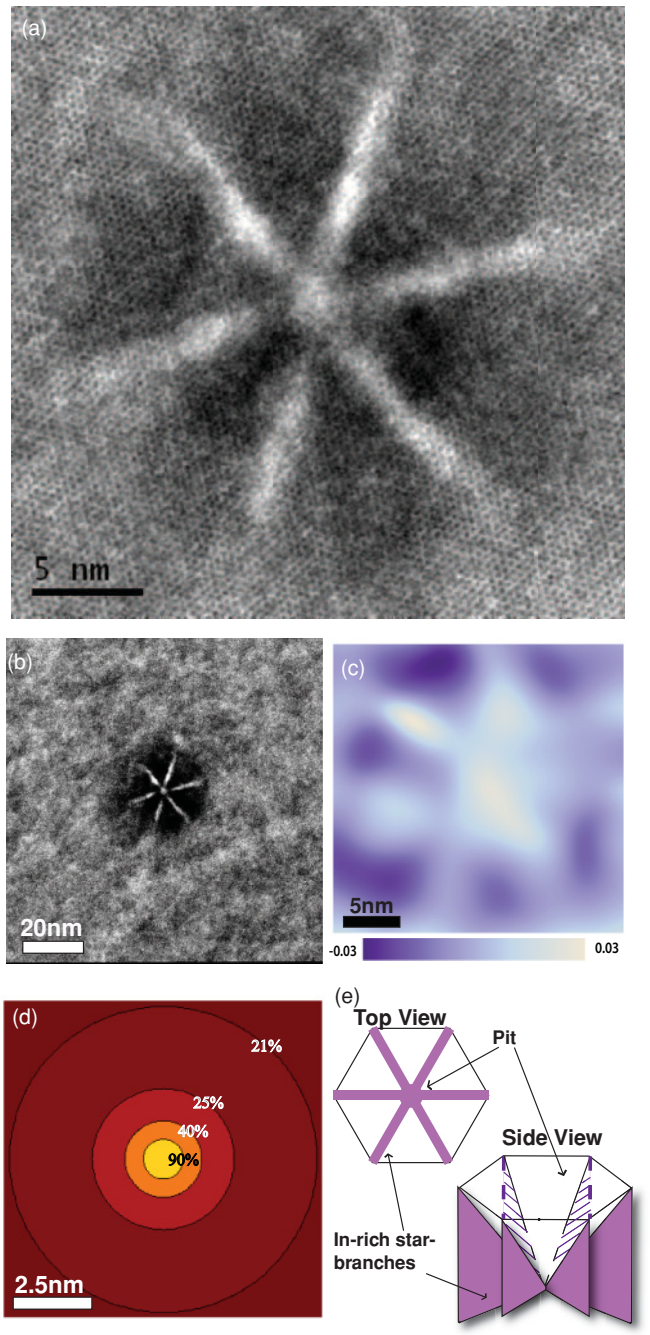

FIG. 4. (Color online) (a) Plan-view HRSTEM-HAADF of a pure-screw dislocation pit. (b) Larger field of view map of (a) showing no antisymmetry in the contrast outside the pit. (c) 2D hydrostatic strain of (a) measured by GPA ($\epsilon_{xx} + \epsilon_{yy}$), showing no discontinuity (meaning the dislocation contains no edge component) and confirming the HAADF bright contrast of (a) is caused by indium. (d) Contour plot of calculated indium distribution around a pure-screw dislocation in $Al_{0.8}In_{0.2}N$ (located at the center of the figure), predicting a sharp, short-range InN segregation on the dislocation core. (e) Perspective representation of the star shapes (in purple) in top and side views.

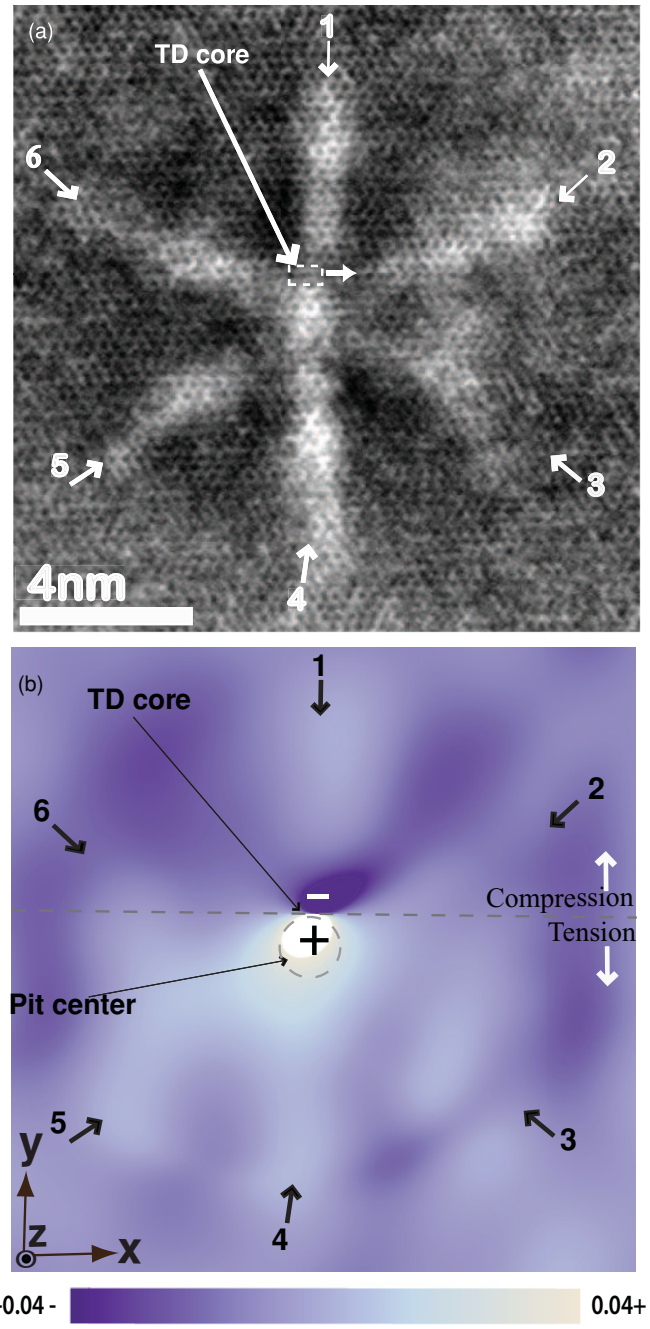

FIG. 5. (Color online) (a) HRSTEM-HAADF map of a mixed dislocation pit, showing the star shape, previously reported to be indium rich.[21] (b) e_{xx} measured by GPA showing that the center of the pit lies immediately on the tensile strain region of the dislocation, indicated by a plus sign. Branches of the star shape appear with a higher lattice parameter than their surroundings and are marked with numbered arrows. Also the dislocation atomic core ring, the star-shaped center, and the compressive and tensile half spaces are indicated on the strain map for further clarity.

numbered in Fig. 5(b), the dislocation core and pit center are indicated with a dotted circle and a labeled arrow, and the tensile and compressive stress half spaces are separated with a dotted line for improved clarity.

The branches appear on the z-contrast map brighter than their environment; they also have a higher lattice parameter from the strain map [Fig. 5(a)], meaning that they are indium

rich. It is visible from the strain map that the star-shape center lies immediately on the tensile side of the dislocation core, indicating that hydrostatic stress affects the star-shape position. Furthermore, from Figs. 5(a) and 5(d), branches 3 and 5 seem to bend toward the axis of maximum stress on the tensile side, and branch 4, which lies on the AMS on the tensile side, yields both a higher z contrast and a higher lattice parameter, meaning it is potentially richer in indium than the rest. On the compressive side, the opposite effect is observed and is clearer in Fig. 6(a), which is the magnified and filtered image of the atomic core ring environment of the TD of Fig. 5, as TD 1 bends away from the AMS, and the dislocation atomic core ring lies on an antisymmetric environment in that direction. Figure 6(b) is a z-contrast intensity profile showing, as in the case of the pure-edge dislocation, that the mixed TD atomic core ring lies on an intensity inflection point along the AMS. This bending phenomenon has been found to be reproducible. The local contrast intensity maximum is located about 1 nm away of the TD atomic core ring. As the star shape and pit centers very likely coincide [Fig. 4(d)], the thickness variation of the pit plays against this asymmetry, since the pit center is thinnest and would yield the smallest HAADF contrast should only thickness variations occur.

Star-shape branches occur on both the the tensile and compressive half spaces of the dislocation; thus their very existence is not hydrostatic-stress related. However, hydrostatic stress appears to affect the position of their center (tensile side), their shape (branch bending), and the composition of their branches.

Figure 7 features a larger scale STEM-HAADF map of four numbered mixed dislocations and an HRTEM image of a subarea. The screw character is recognizable from the pits, and HRTEM shows that dislocations 1, 2, 3, and 4 of Fig. 7 contain an edge component with the extra plane oriented as shown in in the figure. The HRTEM picture of dislocation 1 along with a Burgers circuit is shown in Fig. 7(b).

We see in the STEM-HAADF image [Fig. 7(a)] that the pits are surrounded by an asymmetric environment, a bright, i.e., indium rich, region, and a darker region, i.e., aluminum rich. The contrast aspect is somewhat "rough"; therefore it seems unlikely to be due to bend contours (which are usually smooth and often oscillating). Also, as stated earlier, the sample was

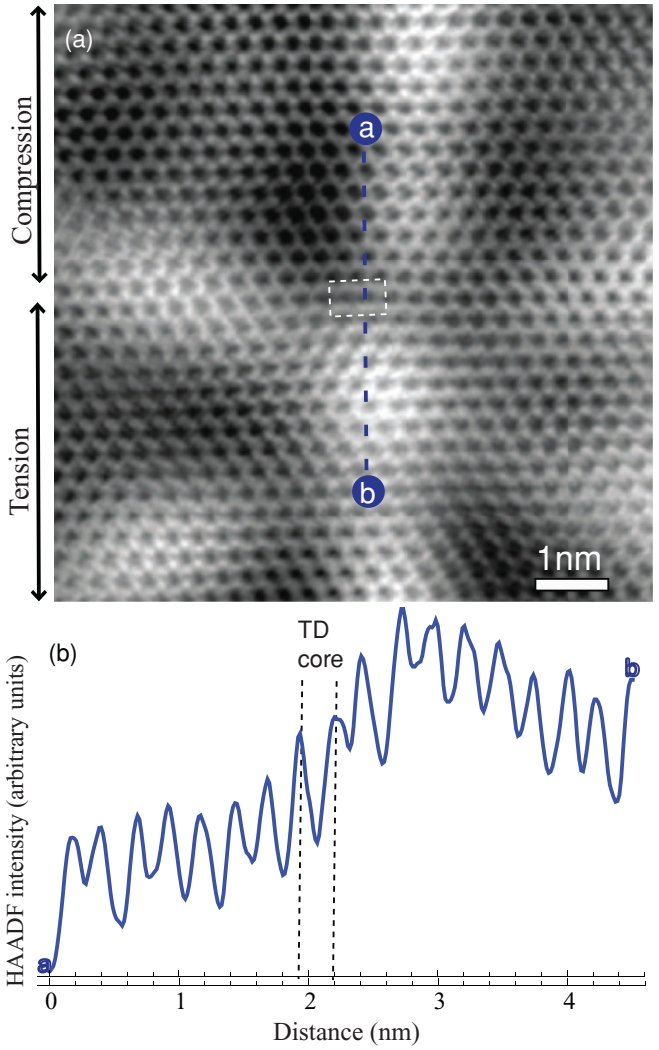

FIG. 6. (Color online) (a) Magnified z-contrast image of the mixed TD core environment of Fig. 5(a), Fourier filtered and sharpened by convolution filter for better clarity. The atomic core ring is indicated by a dotted white rectangle. (b) HAADF intensity profile between points a and b.

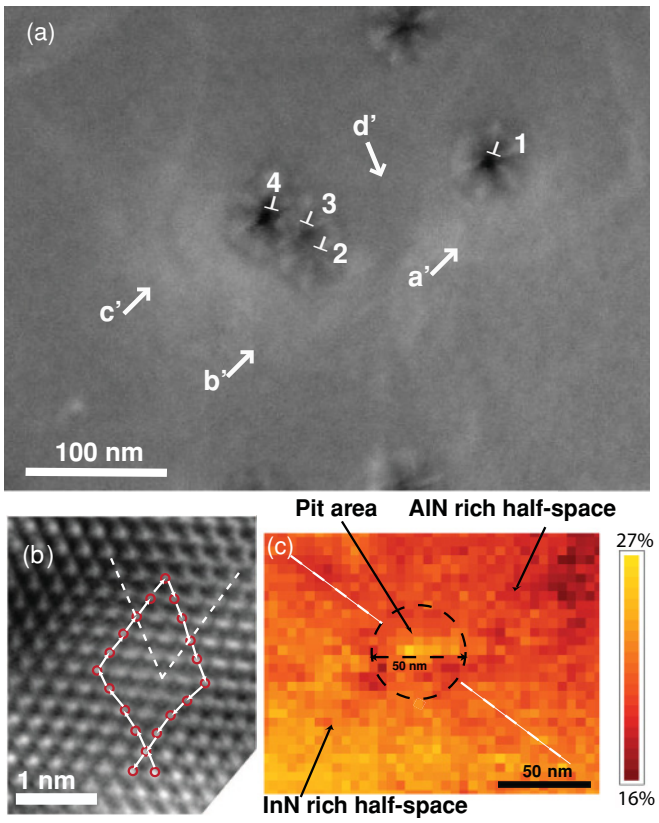

FIG. 7. (Color online) (a) Plan-view STEM-HAADF map of four numbered mixed-type dislocations (identified by their pits and HRTEM), also showing asymmetry in contrast around each dislocation (i.e., an indium-rich half space and an aluminum-rich half space). (b) HRTEM picture of dislocation 1 (Fourier filtered for noise reduction), with a Burgers circuit and the two extra half planes highlighted. (c) InN percentage measured by EDX around a mixed dislocation, where compositional asymmetry is confirmed.

tilted off axis for medium-resolution STEM analysis to avoid channeling and sample bending artifacts.

The bright contrast of regions **a'**–**c'** extends to about 150–200 nm away from the pit and different regions are pointed out by arrows. The correlation [shown in Fig. 7(a)] between bright HAADF contrast and tensile stress region is obvious: The bright out-of-pit region pointed by arrows **b'** and **c'** is in the tensile stress region of dislocations 2, 3, and 4 (i.e., on the opposite side of their extra half plane introduced by their edge component). Also, the bright out-of-pit region **a'** lies on the tensile side of dislocation 1. An interesting point is that the the region of arrows **b'** and **c'** winds around the tensile half space of the pits, while region **a'** is diminished on the left-side region of the pit of dislocation 1 indicated by arrow **d'**. The latter effect is readily interpretable in terms of stress, as region **d'** is under the influence of the compressive stress fields of dislocations 2, 3, and 4, which therefore compensate for the tensile stress of dislocation 1.

This result is definitely confirmed by EDX mapping. Figure 7(c) is an EDX elemental map of indium atomic percentage; aluminum is not shown as it is its exact percentage complement. We clearly see in Fig. 7(c) that the out-of-pit space around the mixed TD (in plan view) is divided into an indium-rich region and an aluminum-rich one. The two regions are separated by a dotted white line and the pit region is indicated by a dotted black circle for clarity. The scan step is of about 5 nm, which is not sufficient to resolve the star shapes of Fig. 5. Nevertheless, an indium peak is observable near the pit center. Outside the pit, as stated earlier, space is divided into an indium-rich and an indium-poor region (separated by the dotted line in the figure). However, the maxima and minima of the indium distribution at the exterior of the pit are located at a few tens of nanometers away of the pit center. The latter effect is not surprising if we consider strain relaxation brought by the introduction of the free surfaces of the pit,[45] canceling out stress at the pit sidewalls and thus shifting the out-of-pit stress maximum and minimum of the dislocation field. Also, anisotropy of surface energetics and of indium incorporation rates with respect to growth facets[46] cannot be ignored in the pit region, as was illustrated by Figs. 4–5. An interesting fact is that indium variation at long distances seems stronger than what the model predicts for an edge-component dislocation, even though further measurements are needed to confirm this discrepancy. Indeed, the model predicts a InN increase by about 2% at 100 nm from the dislocation core, while a variation of about 5% is measured in Fig. 7(c). Also, such a strong long-range variation was not observed for edge dislocations. The underlying cause is an open question; the beginning of an answer may come from the spiral growth generated by the mixed dislocations, possibly coupled with the long surface diffusion lengths of indium adatoms during growth.

V. DISCUSSION

As can be seen from the formulas of the theory section and confirmed by Fig. 2, the composition around a pure-edge dislocation mainly depends on hydrostatic stress, which can cause a total asymmetric segregation on the dislocation core. In fact, the model, and the strain map in Fig. 2(d), are consistent with a 100% InN and AlN segregation on the tensile and compressive regions of the pure-edge TD, respectively. Stress-induced composition modulation around pure-edge TDs is the simplest case and the better matching one to the theory.

Composition in the vicinity of screw-component TDs is complicated by the pit formation, and factors other than stress have to be taken into account to fully understand the causes of the observed elemental fluctuations. On the pit range, the structure seems determined by a complex interplay between shear strain, hydrostatic strain, and surface energetics. Pit centers and dihedral angles were all found to be In rich in the studied sample and were, for this reason, referred to as "star shapes."

Pure-screw TDs do not generate any hydrostatic stress, but their shear stress was shown by calculation to be capable of inducing a very local indium core segregation. The latter fact is consistent with experimental observations, since it has been shown that screw TDs generate pits with indium-rich star shapes, the center of which seems richer in indium.

However, from Figs. 4(a) and 4(c), the indium elemental distribution does not seem to follow the predicted radial decrease [Fig. 4(d)] away of the dislocation on the $\langle 11\bar{2}3\rangle$ paths (star-branch directions).

Mixed-type dislocations behave in a more complex way, having both a edge and screw character. Their In-rich pit (or star-shape) center was shown to lie immediately on the TD tensile side, meaning that it is most likely generated by hydrostatic stress. However, the very existence of their star-shape branches is, as in the case of pure-screw TDs, unlikely stress related since it can be seen from Figs. 5(a) and 5(b) that they occur on both the compressive and tensile half spaces. Nevertheless, hydrostatic stress seems to play a secondary role in the indium content of the star branches, as for example the branches that lie outside the AMS in the tensile stress region of the mixed dislocation of Fig. 5 (i.e., numbers 3 and 4) seem to bend toward the AMS, and branch number 1, which is supposed to lie exactly at the compressive part of the AMS, bends away from it.

Indium segregation on screw-type dislocations was found to be necessary for pit formation in $In_xGa_{1-x}N$ by Northrup *et al.,*[44] since, according to their *ab initio* calculations, GaN terminated surface energy would be too high to introduce the necessary extra sidewalls for strain energy minimization. Our calculations and observations are partially consistent with their remarks: Pit centers were always found to be indium-rich in this study, so if the extra surface of the pits is introduced at their center, the newly created facets would plausibly be indium rich. As the pit grows, it may then be energetically preferable for indium to migrate to the pit dihedral angles and form the observed star shapes. Stress-induced composition modulation may thus provide a plausible explanation to the pit formation origin in InGaN by extrapolation, as the model we used in this paper can be readily applied to $In_xGa_{1-x}N$ and yield very similar predictions.

It can be concluded from our study that surface energetics anisotropy seems to be the most plausible cause of indium segregation on the star-shape branches, but further iterative simulations combining the stress field of a dislocation, surface relaxation, surface energetics from *ab initio* calculations, and a growth model are needed, together with probably some

scanning tunneling microscopy measurements for validation, to definitely elucidate the mechanism of pit formation.

Edge-component dislocations were shown to have a long-range composition effect, as shown for the pure-edge dislocation in Fig. 2 (and by extrapolation of the model since it fits sufficiently well). Mixed dislocations also were shown to have a long-range elemental composition effect outside of the pit regions (Fig. 7) stronger than what is predicted by the model. One important aspect of the implications of the reported results, through their relatively good agreement with the thermodynamic equilibrium based model [especially in the case of a pure-edge TD (Fig. 2)], is that MOVPE is a near thermodynamic equilibrium technique for Group-III nitride growth as predicted by Heying *et al.*[47]

Stress-induced disorder has a potentially major impact on electrical and optical properties of $Al_xIn_{1-x}N$ based components and pseudobinary nitride alloys in general. Stress affects composition on distances of tens of nanometers, enough to affect properties of Bragg mirrors and potentially contribute to explaining the optical disorder reported by Christmann *et al.*[20]

In addition, it can also improve our understanding of defect insensitiveness of indium-containing nitride compounds, and for this, the effect that is emphasized by Figs. 3 and 6 is of major importance. In fact, AlN and GaN have wider band gaps than InN and therefore Al- or Ga-rich regions would act as a potential barriers for charge carriers. Also, In-rich regions will trap carriers and localize excitons. Therefore, since the atomic core ring of edge and mixed component dislocations lies on a composition inflection point, between indium minimum and maximum, charge carrier transmission to the TD atomic core ring (dangling bonds) would be very inefficient, since charges would be either repelled or captured respectively before reaching it. This effect is enforced in mixed TDs, as second indium maxima and minima are present outside of their pits and would therefore also possibly confine and repel charge carriers before even reaching the pit area.

VI. CONCLUSION

We used a set of state-of-the-art techniques, such as z-contrast mapping in an aberration-corrected probe STEM, strain mapping using GPA, medium-resolution EDX, and z contrast, and plan-view sample preparation with a low ion acceleration voltage FIB, and compared the obtained experimental results with elastostatic free energy modeling to draw conclusions about the interplay of stress and composition around threading dislocation in MOVPE $Al_xIn_{1-x}N$. Indium and aluminum peaks lie in the immediate vicinity of the dislocation atomic core ring of a pure-edge TD, and composition fluctuations around it matches well with our calculations; a compositional asymmetry of the same type is found around mixed TD cores. The role of the phenomenon was also highlighted for the pit formation mechanism of mixed-type threading dislocations, and experimental and theoretical evidence was provided for the role of shear stress in InN segregation on pure-screw dislocation cores. Hydrostatic stress was also found responsible for long-range (100–150 nm) fluctuations around edge-type TDs, as expected qualitatively from our calculations. This paper highlights the paramount role of stress in the elemental composition of Group-III nitride ternary alloys.

ACKNOWLEDGMENTS

The authors would like to thank Cécile Hébert (EPFL CIME) for useful discussions. This work is supported by the Swiss National Fund of Scientific Research through Grants No. 200020-122064/1 and No. 200020-113542. Aberration-corrected STEM-HAADF analysis on the CEA-Grenoble FEI-Titan was granted by the French METSA network.

APPENDIX: DERIVATION OF EQUATION (5)

The volume (v) of any crystal unit cell can be calculated as the square root of the determinant of the metric tensor:

$$v = \sqrt{\det\begin{pmatrix} a_1^2 & a_1a_2\cos\psi & a_1a_3\cos\phi \\ a_1a_2\cos\psi & a_2^2 & a_2a_3\cos\theta \\ a_1a_3\cos\phi & a_2a_3\cos\theta & a_3^2 \end{pmatrix}},$$

where θ is the angle between a_2 and a_3, ϕ the angle between a_1 and a_3, and ψ the one between a_1 and a_2. Since a_1 and a_2 are equal in a hexagonal crystal, we obtain

$$v = \sqrt{\det\begin{pmatrix} a_1^2 & \frac{-a_1^2}{2} & 0 \\ \frac{-a_1^2}{2} & a_1^2 & 0 \\ 0 & 0 & a_3^2 \end{pmatrix}} = \frac{\sqrt{3}}{2}a_1^2a_3 = \frac{h\sqrt{3}}{2}a_1^3,$$

where h is the hexagonal a_3/a_1 ratio, whose ideal value is 1.633. The h values of InN and AlN (as presented by Table I) deviate by 1.29% and 1.96% from the ideal value, possibly due to spontaneous polarization. The h value varies negligibly between AlN and InN (0.66%). We therefore assume a constant h value for AlN, InN, and their intermediate alloys. We approximate the volume change undergone by the elastic inhomogeneity (ΔV) of indium content $\mathbf{c}$ in an AlInN alloy of indium content $\mathbf{c_0}$—using Eq. (2) and assuming h constant—as

$$\Delta V \cong \alpha(v(\mathbf{c}) - v(\mathbf{c_0}))$$

and

$$\Delta V = \frac{h\sqrt{3}}{2}\left[a_1^{\mathrm{inc}\,3}(\mathbf{c}) - a_1^3(\mathbf{c_0})\right],$$

where ΔV is the volume change undergone by the elastic inhomogeneity, and $v(\mathbf{c})$ and $v(\mathbf{c_0})$ are the volumes of unit cells of indium contents $\mathbf{c}$ and $\mathbf{c_0}$, respectively. Hence,

$$\frac{h\sqrt{3}}{2}\left[a_1^{\mathrm{inc}\,3}(\mathbf{c}) - a_1^3(\mathbf{c_0})\right] \cong \alpha\frac{h\sqrt{3}}{2}\left[a_1^3(\mathbf{c}) - a_1^3(\mathbf{c_0})\right].$$

Simplifying, we obtain

$$a_1^{\mathrm{inc}}(\mathbf{c}) \cong \sqrt[3]{\alpha\, a_1^3(\mathbf{c}) + a_1^3(\mathbf{c_0})(1-\alpha)}.$$

As $a_1 = a_2$ and a_3 can be substituted, in our approximation, by ha_1, the equation can be generalized for all three lattice parameters, giving Eq. (5):

$$a_i^{\mathrm{inc}}(\mathbf{c}) \cong \sqrt[3]{\alpha\, a_i^3(\mathbf{c}) + a_i^3(\mathbf{c_0})(1-\alpha)}.$$

*anas.mouti@epfl.ch

[1] K. Hirmatsu, S. Itoh, H. Amano, I. Akasaki, N. Kuwano, T. Shiraishi, and K. Oki, J. Cryst. Growth (1991).

[2] S. Nakamura, S. Pearton, and G. Fasol, Meas. Sci. Technol. **12**, 755 (2001).

[3] O. Ambacher, J. Phys. D **31**, 2653 (1998).

[4] S. Christopoulos, G. Baldassarri, H. V. Hogersthal, A. J. D. Grundy, P. G. Lagoudakis, A. V. Kavokin, J. J. Baumberg, G. Christmann, R. Butté, E. Feltin *et al.*, Phys. Rev. Lett. **98**, 126405 (2007).

[5] R. Butté, J.-F. Carlin, E. Feltin, M. Gonschorek, S. Nicolay, G. Christmann, D. Simeonov, A. Castiglia, J. Dorsaz, H. Buehlmann *et al.*, J. Phys. D **40**, 6328 (2007).

[6] J.-F. Carlin and M. Ilegems, Appl. Phys. Lett. **83**, 668 (2003).

[7] M. Gonschorek, J.-F. Carlin, E. Feltin, M. A. Py, N. Grandjean, V. Darakchieva, B. Monemar, M. Lorenz, and G. Ramm, J. Appl. Phys. **103**, 093714 (2008).

[8] S. Nicolay, J.-F. Carlin, E. Feltin, R. Butté, M. Mosca, N. Grandjean, M. Ilegems, M. Tchernycheva, L. Nevou, and F. H. Julien, Appl. Phys. Lett. **87**, 111106 (2005).

[9] S. F. Chichibu *et al.*, Nature Mater. **5**, 810 (2006).

[10] S. Nakamura, Science **281**, 956 (1998).

[11] S. Chichibu, T. Azuhata, T. Sota, and S. Nakamura, Appl. Phys. Lett. **69**, 4188 (1996).

[12] Y. Narukawa, Y. Kawakami, M. Funato, S. Fujita, S. Fujita, and S. Nakamura, Appl. Phys. Lett. **70**, 981 (1997).

[13] T. M. Smeeton, M. J. Kappers, J. S. Barnard, M. E. Vickers, and C. J. Humphreys, Appl. Phys. Lett. **83**, 5419 (2003).

[14] F. C. Frank, Acta Crystallogr. **4**, 497 (1951).

[15] I.-H. Kim, H.-S. Park, Y. Park, and T. Kim, Appl. Phys. Lett. **73**, 1634 (1998).

[16] Z. L. Miao, T. J. Yu, F. J. Xu, J. Song, C. C. Huang, X. Q. Wang, Z. J. Yang, G. Y. Zhang, X. P. Zhang, D. P. Yu *et al.*, Appl. Phys. Lett. **95**, 231909 (2009).

[17] L. Zhou, M. R. McCartney, D. J. Smith, A. Mouti, E. Feltin, J. F. Carlin, and N. Grandjean, Appl. Phys. Lett. **97**, 161902 (2010).

[18] A. N. Bright, N. Sharma, and C. J. Humphreys, J. Electron. Microsc. **50**, 489 (2001).

[19] H. K. Cho, J. Y. Lee, G. M. Yang, and C. S. Kim, Appl. Phys. Lett. **79**, 215 (2001).

[20] G. Christmann, D. Simeonov, R. Butté, E. Feltin, J.-F. Carlin, and N. Grandjean, Appl. Phys. Lett. **89**, 261101 (2006).

[21] T. Kehagias, G. P. Dimitrakopulos, J. Kioseoglou, H. Kirmse, C. Giesen, M. Heuken, A. Georgakilas, W. Neumann, T. Karakostas, and P. Komninou, Appl. Phys. Lett. **95**, 071905 (2009).

[22] L. Zhou, D. J. Smith, M. R. McCartney, D. S. Katzer, and D. F. Storm, Appl. Phys. Lett. **90**, 081917 (2007).

[23] S.-L. Sahonta, G. P. Dimitrakopulos, T. Kehagias, J. Kioseoglou, A. Adikimenakis, E. Iliopoulos, A. Georgakilas, H. Kirmse, W. Neumann, and P. Komninou, Appl. Phys. Lett. **95**, 021913 (2009).

[24] J. Eshelby, Proc. R. Soc. London **241**, 376 (1957).

[25] J. Hirth and J. Lothe, Theory of Dislocations (Krieger, Malabar, 1982).

[26] J. Eshelby, W. Read, and W. Shockley, Acta Metall. **1**, 251 (1953).

[27] J. H. Edgar, (INSPEC, London, 1994).

[28] K. Lorenz, N. Franco, E. Alves, I. M. Watson, R. W. Martin, and K. P. O'Donnell, Phys. Rev. Lett. **97**, 085501 (2006).

[29] K. Tsubouchi, K. Sugai, and N. Mikoshiba, IEEE Trans. Sonics Ultrason. **1**, 375 (1981).

[30] A. Sheleg and V. Savastenko, Inorg. Mater. (USSR)**15**, 1598 (1979).

[31] M. J. Hÿtch, E. Snoeck, and R. Kilaas, Ultramicroscopy **74**, 131 (1998).

[32] J. Rouvière and E. Sarigiannidou, Ultramicroscopy **106**, 1 (2005).

[33] Z. Liliental-Weber and D. Cherns, J. Appl. Phys. **89**, 7833 (2001).

[34] S. Gradecak, V. Wagner, M. Ilegems, T. Riemann, J. Christen, and P. Stadelmann, Appl. Phys. Lett. **80**, 2866 (2002).

[35] H. M. Zbib, T. D. de la Rubia, M. Rhee, and J. Hirth, J. Nucl. Mater. **276**, 154 (2000).

[36] P. Kirkby, IEEE J. Quantum Electron. **11**, 562 (1975).

[37] Y. Hasegawa, T. Egawa, T. Jimbo, and M. Umeno, Jpn. J. Appl. Phys. **35**, 5637 (1996).

[38] S. M. Hu, Appl. Phys. Lett. **31**, 53 (1977).

[39] Y. Xin, S. J. Pennycook, N. D. Browning, P. D. Nellist, S. Sivananthan, F. Omnes, B. Beaumont, J. P. Faurie, and P. Gibart, Appl. Phys. Lett. **72**, 2680 (1998).

[40] S. Kret, P. Dluzewski, G. Maciejewski, V. Potin, J. Chen, P. Ruterana, and G. Nouet, Diam. Relat. Mater. **11**, 910 (2002).

[41] M. Hÿtch, J.-L. Putaux, and J.-M. Pénisson, Nature (London) **423**, 270 (2003).

[42] O. L. Krivanek, M. F. Chisholm, V. Nicolosi, T. J. Pennycook, G. J. Corbin, N. Dellby, M. F. Murfitt, C. S. Own, Z. S. Szilagyi, M. P. Oxley *et al.*, Nature (London) **464**, 571 (2010).

[43] H. Lei, J. Chen, and P. Ruterana, Appl. Phys. Lett. **96**, 161901 (2010).

[44] J. E. Northrup, L. T. Romano, and J. Neugebauer, Appl. Phys. Lett. **74**, 2319 (1999).

[45] T. L. Song, J. Appl. Phys. **98**, 084906 (2005).

[46] A. Chakraborty, S. Keller, C. Meier, B. A. Haskell, S. Keller, P. Waltereit, S. P. DenBaars, S. Nakamura, J. S. Speck, and U. K. Mishra, Appl. Phys. Lett. **86**, 031901 (2005).

[47] B. Heying, E. J. Tarsa, C. R. Elsass, P. Fini, S. P. DenBaars, and J. S. Speck, J. Appl. Phys. **85**, 6470 (1999).